Check for updates

IET Smart Grid

WILEY

The Institution of Engineering and Technology

ORIGINAL RESEARCH OPEN ACCESS

Co-Simulation Microgrid With Distributed Control Based on a Multi-Agent System and Communication With Adaptive Update Rate

Daniel Leocádio Fernandes[1] | Guilherme Márcio Soares[1] | Janaína Gonçalves de Oliveira[1,2]

[1]Departamento de Engenharia Elétrica, Universidade Federal de Juiz de Fora, Juiz de Fora, Brazil | [2]Department of Electrical Engineering, Uppsala University, Uppsala, Sweden

Correspondence: Daniel Leocádio Fernandes (daniel.leocadio@estudante.ufjf.br)

Received: 29 July 2025 | **Revised:** 13 November 2025 | **Accepted:** 26 December 2025

Keywords: distributed control | microgrid design | multi-agent systems | power system simulation

ABSTRACT

This study presents a distributed control system for a multiagent co-simulation environment, designed to regulate a direct current (DC) bus voltage in a grid-connected microgrid (MG). The system adopts a client/server architecture, enabling seamless communication in a network of interconnected components integrated into a MG while implementing adaptive update-rate communication to optimise data exchange efficiency. A multiagent system (MAS) orchestrates interactions between power converters, ensuring seamless operation of a DC microgrid powered by photovoltaic (PV) arrays, a battery storage system and an inverter/rectifier converter connected to the main grid. The framework integrates Python, TCP/IP sockets and industry-standard simulators (PLECS, PSIM and RTDS) to create a co-simulation environment. Key results demonstrate effective DC bus voltage regulation and battery voltage control (used as a proxy for SoC), ensuring system stability under varying operating conditions. The proposed approach enhances system responsiveness through adaptive update rate communication, which dynamically adjusts data transmission among agents and the MAS based on real-time network conditions. This improvement is evidenced by a reduction of approximately 13% in the average settling time of the secondary control layer, from 267 s to 232.4 s, when the communication medium delay varies during system operation under the adaptive update rate, compared with the fixed update rate scenario. These results highlight the superior dynamic performance of the hierarchical control strategy at the supervisory level.

1 | Introduction

Renewable energy has become a significant area of research, driving the exploration of innovative methodologies for power generation. Within this domain, microgrids (MGs) have emerged as a viable solution for sustainable energy distribution, offering enhanced reliability and efficiency [1]. Furthermore, MGs integrated through co-simulation—a computational approach that synchronises multiple simulation tools within an unified framework—enable robust modelling, design and optimisation of complex energy systems [2]. However, despite its advantages, co-simulation faces significant challenges, particularly in developing effective communication frameworks that ensure seamless interaction and data exchange between diverse simulators and subsystems. In ref. [3] the authors employs Java Agent DEvelopment Framework (JADE) as a multiagent system alongside the MACSimJX to facilitate the communication with physical power system simulated by MATLAB/Simulink. Communication infrastructure serves as the backbone of microgrid systems, interconnecting all components. Both wired and wireless implementations are susceptible to performance degradation in low-quality network environments [4]. In ref. [5],

This is an open access article under the terms of the Creative Commons Attribution-NonCommercial-NoDerivs License, which permits use and distribution in any medium, provided the original work is properly cited, the use is non-commercial and no modifications or adaptations are made.

© 2026 The Author(s). *IET Smart Grid* published by John Wiley & Sons Ltd on behalf of The Institution of Engineering and Technology.

the authors propose a general co-simulation-based platform for validating distributed algorithms with cyber-physical energy systems (CPES) integration. To address uncertainties in communication network, the platform employs direct agent communication, allowing neighbouring agents to exchange signals. In their work, ref. [6] investigate various modelling approaches for local energy communities (LECs), including a distributed control layer architecture. In this framework, primary controllers handle the localised operation of individual components, whereas secondary controllers coordinate energy flow at a system-wide level. The proposed distributed framework employs agent-based communication, where each agent interacts only with its immediate neighbours.

The authors in ref. [7] propose a co-simulation framework that enhances microgrid power sharing through flexible communications and a resilient control algorithm, addressing challenges such as cyber vulnerabilities and latency. By implementing model-based predictive control and utilising software-defined networking (SDN), the framework achieves rapid communication and effective regulation of frequency and voltage deviations, demonstrating strong performance even under cyber-attack scenarios. In ref. [8] the authors focus on parking lots equipped with fast public charging stations, employing a hierarchical aggregation approach. The authors analyse a multiagent system composed of intelligent electronic devices (IEDs) installed across the grid—particularly at critical branches susceptible to overloading from electric vehicles charging demand—along with distributed agents that facilitate decentralised control. The proposed distributed control algorithm effectively manages network congestion while incorporating a local regulation function to mitigate voltage fluctuations caused by charging activities. In ref. [9], the authors propose a framework that eliminates manual code modifications—DecompositionJ (DEterministic, COncurrent Multi-PrOcesssing SImulaTION for Java programs). According to the authors, this framework reduces the cost of developing and maintaining models for target software.

The authors aforementioned have studied multiagent systems (MASs), power simulators, co-simulators and communication simulators software as summarised in Table 1.

This study introduces a distributed control system for a DC microgrid within a co-simulation framework that combines industry-standard simulators—PLECS, PSIM and RTDS—in a heterogeneous environment encompassing both real-time and non-real-time platforms as illustrated in Figure 1. This hybrid configuration reflects real-world operational challenges and demonstrates the capability of the multiagent system (MAS) to coordinate strongly heterogeneous systems while maintaining stability under diverse execution profiles. A key innovation of this work is the implementation of an adaptive update rate algorithm that dynamically adjusts communication frequency based on network conditions, ensuring robust performance even during simulated communication degradation events. Furthermore, the proposed approach includes a comparative analysis between fixed and adaptive update rates, highlighting significant improvements in responsiveness and reliability. These enhancements, together with the integration of real-time and non-real-time simulators, position the framework as a scalable and resilient solution for distributed control in DC microgrids.

The proposed system employs Python and TCP/IP sockets [10, 11] as the communication backbone for the multiagent system (MAS), enabling efficient agent-based interaction and supporting the adaptive update rate algorithm. This choice is motivated not only by Python's extensive ecosystem of mature libraries and its suitability for rapid prototyping but also by the fact that the MAS imposes relatively low computational demand. All heavy numerical calculations are performed within the simulators

TABLE 1 | Summary on the commented literature works.

Ref.	Summary	MAS	Physical system simulator	Network systems
[2]	Authors develop a co-simulation testbed	JADE	DigSilent power-factory	OMNET++ and INET
[3]	Authors develop an EMS to maintain the power balance in the microgrid	JADE	MATLAB/Simulink	MAC-SimJX
[5]	A general co-simulation based platform to validate distributed algorithms with cyber-physical system integration	Cyber system	PyPower	Cyber system
[6]	Three LEC models with community markets, highlighting the distributed control	JADE	DigSilent	OMNET++
[7]	A co-simulation framework that enhances microgrid power sharing through flexible communications	Not used	MATLAB/Simulink	GNS3
[8]	Researchers examine a MAS using IEDs deployed on critical grid branches prone to EV charging overloads	Not used	EMTP	OMNeT++
[9]	The authors proposed framework based upon HLA standard	JADE	PSCAD	OPNET
This work	A distributed control system tested in a co-simulation framework, maintaining diverse update rates across the MAS.	Python	RSCAD/RTDS, PSIM and PLECS	NS3

25152947, 2026, 1, Downloaded from https://ietresearch.onlinelibrary.wiley.com/doi/10.1049/stg2.70054 by Uppsala University Library, Wiley Online Library on [04/08/2026]. See the Terms and Conditions (https://onlinelibrary.wiley.com/terms-and-conditions) on Wiley Online Library for rules of use; OA articles are governed by the applicable Creative Commons License

(PLECS, PSIM and RTDS), whereas the MAS acts primarily as a high-level orchestrator responsible for message wrapping, synchronisation and adaptive update rate control. For these orchestration tasks, which operate at millisecond-level update rates, Python provides adequate performance with minimal overhead and significantly reduces development time. TCP/IP sockets complement this by offering a standardised and reliable protocol for message exchange, ensuring interoperability across heterogeneous platforms. Together, these technologies allow the MAS to dynamically adjust communication frequency in response to network conditions, maintaining system stability even under adverse scenarios such as simulated communication degradation. The manuscript offers comprehensive documentation of the co-simulation process, including system architecture, design methodology and performance evaluation. These features position the proposed framework as a flexible and scalable solution for distributed control in DC microgrids operating in hybrid simulation environments, delivering practical insights for real-world implementations and future developments in complex energy systems.

This article is structured into four main sections following the conventional IMRAD (Introduction, Methods, Results and Discussion) format. The current Section 1, which provides background information, states the research problem, and outlines the study's objectives. The Section 2 details the experimental design, procedures and analytical techniques used to conduct the research. The Section 3 presents the key findings, supported by figures describing the experiment outputs. Finally, the Section 4 summarises the main outcomes, discusses their implications and suggests potential future research directions. This logical organisation ensures clarity and facilitates systematic comprehension of the study.

2 | Methods

2.1 | System Under Study

The co-simulation environment models a small village powered by a DC microgrid connected to the power grid. The system includes residential units housing various power converters, photovoltaic (PV) panels and a battery bank operating at 720 V. The DC bus voltage is regulated at 900 V by a bidirectional converter. Figure 2 illustrates the system, which consists of:

- A bidirectional DC/DC converter and a battery bank;
- A photovoltaic panel controlled by a DC converter;
- An inverter (DC/AC converter) supplying energy to the consumer;
- An inverter/rectifier that can supply or draw power from the DC bus connected to the grid.

2.2 | Power Converter Simulation

The system under study models a small village supplied by a DC microgrid designed to provide reliable energy to residential loads. The DC bus architecture is adopted to ensure efficient integration of renewable energy sources and energy storage, simplifying control and enhancing stability under variable generation and load conditions [12].

The microgrid includes several key components interconnected through the DC bus, which is regulated at 900 V. These components are as follows:

- A bidirectional DC/DC converter connected to a battery bank (720 VDC nominal voltage) that manages energy storage and release based on system demands and generation surplus;

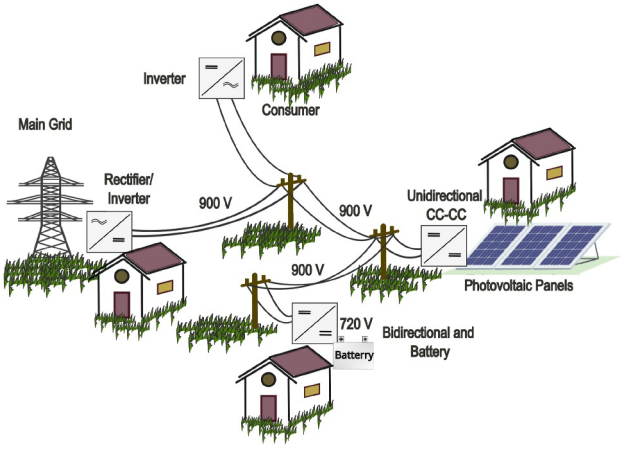

FIGURE 2 | Illustration of the system under study.

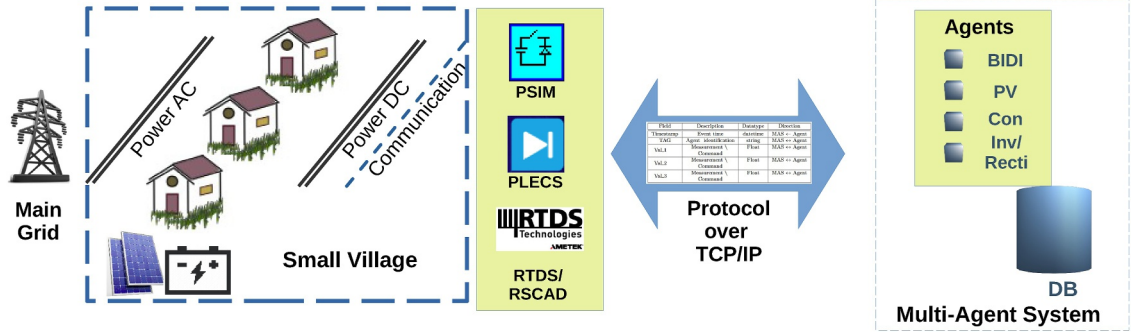

FIGURE 1 | Simulation environment—Overview.

25152947, 2026, 1, Downloaded from https://ietresearch.onlinelibrary.wiley.com/doi/10.1049/stg2.70054 by Uppsala University Library, Wiley Online Library on [04/08/2026]. See the Terms and Conditions (https://onlinelibrary.wiley.com/terms-and-conditions) on Wiley Online Library for rules of use; OA articles are governed by the applicable Creative Commons License

— A photovoltaic (PV) system equipped with a DC/DC buck converter featuring maximum power point tracking (MPPT) to optimise solar energy capture;

— An inverter/rectifier that interfaces with the main power grid, enabling power exchange (import/export) and ensuring the microgrid's stability;

— A consumer-side inverter (DC/AC converter) that supplies AC loads in the residential units.

The battery bank capacity is described in Table 2, supporting the system during periods of low solar generation or high demand. The PV panels generation is dimensioned according to Table 2 under standard conditions, with real-time variations based on solar irradiation.

To ensure realistic and accurate simulation, the system model incorporates the operational dynamics of each power converter. The converters are simulated using different software platforms (PLECS, PSIM and RTDS) to capture their unique characteristics and control strategies. A multiagent system (MAS) coordinates these elements, managing power flow, communication and adaptive update rates. Figure 2 presents a theoretical overview of the system under study, highlighting the interconnections between the converters, the grid and the main setup data of the system.

To validate the effectiveness of the proposed co-simulation framework, the power converters were simulated across multiple software environments, each selected for its specific modelling capabilities and simulation performance. This approach enables the integration of detailed converter dynamics while addressing the challenges of coordinating real-time and non-real-time systems.

The PV converter (buck topology) was simulated in PSIM, including maximum power point tracking (MPPT) control, to optimise energy harvesting under varying solar conditions. The consumer-side inverters were also simulated in PSIM, capturing their dynamic responses to the residential load profiles.

The bidirectional DC/DC converter (Bidi), connected to the battery bank, was simulated in PLECS. This simulation focuses on the regulation of the DC bus voltage at 900 *VDC* and the management of the battery voltage at 720 *VDC*, as listed in Table 2, ensuring balanced charging and discharging cycles.

The inverter/rectifier (INV), responsible for interfacing the microgrid with the main grid, was simulated in RTDS. Its real-time simulation environment enables accurate representation of power exchange processes and grid-supporting functions.

TABLE 2 | System parameters.

Component	Value
Battery bank	17 *kAh* at 720 *VDC*
PV	31.5 *kW*
DC bus	900 *VDC*

To ensure consistent and efficient operation in the co-simulation, all converters were modelled using average models. This modelling choice allowed PLECS and PSIM to operate with a simulation timestep comparable to that of RTDS, ensuring proper synchronisation. Figure 3 shows the PV Converter average model main circuit. In this figure, the voltage applied by the photovoltaic array to the circuit is represented by the controlled source, signal *vpvp*, with the reference point *Vt* at its positive terminal. The signals *s*1, *s*2 and *Vt* are obtained from Equation (2). Let:

$$\begin{cases} s1(t) = d; \\ s2(t) = 1 - d; \\ d = \dfrac{m+1}{2}. \end{cases} \tag{1}$$

From the expressions in Equation (1), leads to:

$$\begin{cases} Vt(t) = V_{PV}.s1(t); \\ i_{s1}(t) = s1(t).i_{l_0}(t); \\ i_{s2}(t) = -s2(t).i_{l_0}(t). \end{cases} \tag{2}$$

Subsequently, the average models of the previous expressions are obtained.

$$\begin{cases} \overline{V_t} = V_{PV}.d; \\ \overline{i_{s1}} = d.\overline{i_{l_0}}; \\ \overline{i_{s2}} = -(1-d).\overline{i_{l_0}}. \end{cases} \tag{3}$$

Finally, substituting Equation (1) into Equation (3), the control equation for the average model of the buck converter is obtained:

$$\begin{cases} \overline{V_t} = V_{PV}.\dfrac{m+1}{2}; \\ \overline{i_{s1}} = \dfrac{m+1}{2}.i_{l_0}; \\ \overline{i_{s2}} = -\dfrac{1-m}{2}.i_{l_0}. \end{cases} \tag{4}$$

Figure 4 illustrates the converter control signals obtained from Equation (4).

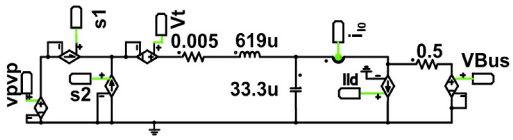

FIGURE 3 | PV converter average model.

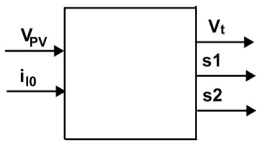

FIGURE 4 | Circuit composition of the control signal generators for the controlled sources of the average model of the unidirectional DC/DC converter.

25152947, 2026, 1, Downloaded from https://ietresearch.onlinelibrary.wiley.com/doi/10.1049/stg2.70054 by Uppsala University Library, Wiley Online Library on [04/08/2026]. See the Terms and Conditions (https://onlinelibrary.wiley.com/terms-and-conditions) on Wiley Online Library for rules of use; OA articles are governed by the applicable Creative Commons License

Figure 5 illustrates the average model circuit of the bidirectional converter coupled to the energy storage device, the battery. This converter controls the voltage level on the DC bus.

The control signals for the controlled sources in Figure 5 are generated from the Equation (6) as illustrated in Figure 6, as follows:

$$\begin{cases} V_t(t) = vt_c(t); \\ vt_c(t) = V_c(t).d; \\ it_batt(t) = i_{batt}(t).d. \end{cases} \quad (5)$$

By setting $d = \frac{m+1}{2}$ in Equation (5), it is obtained the equations for the control signals of the controlled sources in the average model V_t, vt_c and it_batt.

$$\begin{cases} \overline{V}t_c = \dfrac{m+1}{2}.V_c \\ \overline{it}_batt = \dfrac{m+1}{2}.I_{batt} \end{cases} \quad (6)$$

The average model of the load is illustrated in Figure 7. The variable v_{barr} represents the DC bus voltage reference, and the sensor i_s provides the information of the current consumed by the load, R_1.

The capacitor of 2 μF, located in parallel with $R1$, aims to filter high-frequency components for the reading of the sensor i_s, providing stable current measurements consumed by the load.

The INV converter, responsible for interfacing the microgrid with the main grid, employs the dynamic average value model (DAVM) component, available in the RTDS simulator. This component, illustrated in Figure 8, is adopted in the environment under study.

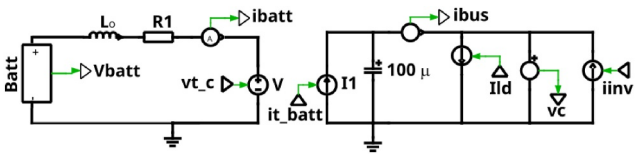

FIGURE 5 | Average model of the bidirectional DC-DC converter.

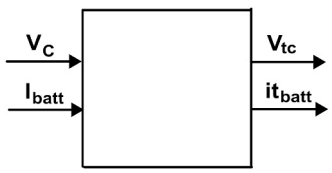

FIGURE 6 | Control signals of the controlled sources of the bidirectional converter average model.

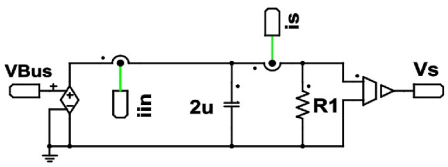

FIGURE 7 | Average model of the load.

The DAVM component replaces the switched voltage source converter (VSC) with controlled voltage and current sources that represent the average dynamics of the VSC control. The AC voltage is obtained from sinusoidal control reference signals defined within the simulator. The operation of the DAVM can be configured using user-defined control signals or computed based on the power balance principle [13].

The deliberate use of different simulation platforms for specific converters creates a hybrid co-simulation environment that reflects the real-world challenges in microgrid operation, including heterogeneous update rates and execution profiles. This setup provides a comprehensive testbed for evaluating the MAS's ability to coordinate system components and maintain robust performance.

2.3 | Communication Structure

The multiagent system (MAS) enables bidirectional communication between subsystems via TCP/IP sockets. Each agent—specifically, the bidirectional converter (Bidi), inverter/rectifier (INV), photovoltaic converter (PV) and consumer-side inverter (Con)—exchanges measurements and control commands with the MAS.

The application-layer [14] protocol is structured in data packets containing the following fields:

- Time Stamp: Indicates the occurrence time of the message;
- TAG: Identifies the sending or receiving agent;
- Val_1, Val_2, Val_3: Represent measurements (agent → MAS) or control commands (MAS → agent).

Table 3 depicts the layout of these data packets, which ensures consistent communication across the co-simulation framework.

Communication channel degradation, such as increased delays, may arise under adverse network conditions. To assess these scenarios, the NS-3 simulator [15] was used to model network performance feeding the system with delay information in order to evaluate its impact.

To ensure robust communication in the presence of time-varying network conditions, a dynamic update rate mechanism was developed and implemented in the multiagent system (MAS). This strategy allows the MAS to regulate the

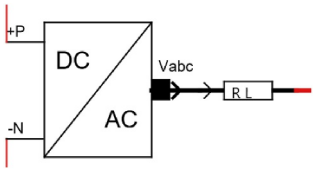

FIGURE 8 | Dynamic average value model.

25152947, 2026, 1, Downloaded from https://ietresearch.onlinelibrary.wiley.com/doi/10.1049/stg2.70054 by Uppsala University Library, Wiley Online Library on [04/08/2026]. See the Terms and Conditions (https://onlinelibrary.wiley.com/terms-and-conditions) on Wiley Online Library for rules of use; OA articles are governed by the applicable Creative Commons License

communication frequency of each agent individually, based on observed message delivery times, aiming to maintain both communication reliability and overall system stability.

Let each agent $i \in \{1, 2, ..., n\}$ be associated with an update period $UP_k^i \in \mathbb{R}_{>0}$ at the discrete time step k. The update period represents the expected interval between consecutive messages received from agent i and is defined as the inverse of the update frequency f_k^i:

$$UP_k^i = \frac{1}{f_k^i}. \tag{7}$$

The MAS monitors the actual time interval between two successive messages as follows:

$$\Delta t_k^i = t_k^i - t_{k-1}^i, \tag{8}$$

where t_k^i and t_{k-1}^i are the reception timestamps of the current and previous messages from agent i, respectively.

An adaptive algorithm adjusts the update period based on the comparison between Δt_k^i and the configured UP_k^i. The update rule is defined as follows:

$$UP_{k+1}^i = \begin{cases} \max\left(UP_k^i - \alpha, UP_{\min}\right), & \text{if } \Delta t_k^i \le UP_k^i, \\ \min\left(UP_k^i + \alpha, UP_{\max}\right), & \text{if } \Delta t_k^i > UP_k^i, \end{cases} \tag{9}$$

where

- $\alpha > 0$: adaptation step size (in seconds);
- $UP_{\min}, UP_{\max} \in \mathbb{R}_{>0}$: lower and upper bounds on the update period.

The algorithm is initialised with a default value:

$$UP_0^i = UP_{\text{default}}, \tag{10}$$

and enforces the constraint:

$$UP_{\min} \le UP_k^i \le UP_{\max}, \quad \forall k \in \mathbb{N}. \tag{11}$$

The mechanism operates independently for each agent, enabling heterogeneous communication rates across the system. When the observed interval Δt_k^i is smaller than or equal to the configured period UP_k^i, the MAS reduces the update period (i.e., increases the update frequency), favouring responsiveness. Conversely, when $\Delta t_k^i > UP_k^i$, the update period is increased, reducing communication load and avoiding message overlap or congestion.

The communication protocol relies on a client-server architecture [16], where the MAS (server) sequentially processes and responds to agent messages, ensuring determinism and preventing simultaneous access conflicts.

Figure 9 illustrates the update rate regulation process. For each agent i, the MAS records timestamps $t_i^{(k-1)}$ and $t_i^{(k)}$ corresponding to two successive messages. The measured interval Δt_k^i determines whether the update period UP_k^i should be increased or decreased as per Equation (9). The diagram also indicates:

- UR (1...n): current update rates for each of the n agents;
- PT: processing time required by the MAS for each communication cycle;
- $t0.0$ and $t0.1$: timestamps from Agent 1, with $\Delta t = t0.1 - t0.0$;
- $tN.0$ and $tN.1$: analogous timestamps from Agent N.

This level of granularity allows the MAS to assess communication performance at the agent level and to proactively mitigate instability or latency. For instance, if the MAS detects that $\Delta t_k^1 > UP_k^1$, the algorithm commands Agent 1 to reduce its update frequency by increasing its update period, helping to maintain synchronisation and avoid channel saturation.

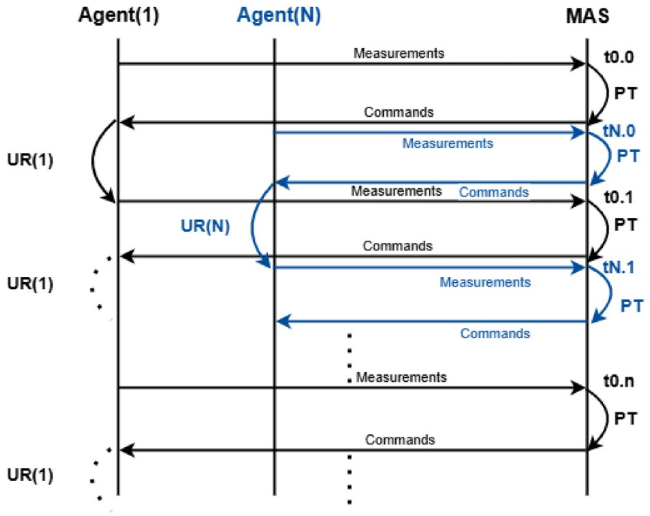

FIGURE 9 | Update period adjustment mechanism based on agent-specific communication delays.

TABLE 3 | Communication protocol between agents and the MAS.

Field	Description	Datatype	Direction
Timestamp	Event time	Datetime	MAS ← agent
TAG	Agent identification	String	MAS ↔ agent
Val_1	Measurement \ command	Float	MAS ↔ agent
Val_2	Measurement \Command	Float	MAS ↔ agent
Val_3	Measurement \ command	Float	MAS ↔ agent

25152947, 2026, 1, Downloaded from https://ietresearch.onlinelibrary.wiley.com/doi/10.1049/stg2.70054 by Uppsala University Library, Wiley Online Library on [04/08/2026]. See the Terms and Conditions (https://onlinelibrary.wiley.com/terms-and-conditions) on Wiley Online Library for rules of use; OA articles are governed by the applicable Creative Commons License

2.4 | Multi-Agent System (MAS)

The MAS coordinates the overall system operation, exchanging messages asynchronously with individual agents. A PostgreSQL database stores exchanged data for future analysis. The MAS control algorithm, shown in Figure 10, ensures system stability by adjusting the inverter's operation based on the battery voltage level (*Batt Volt*).

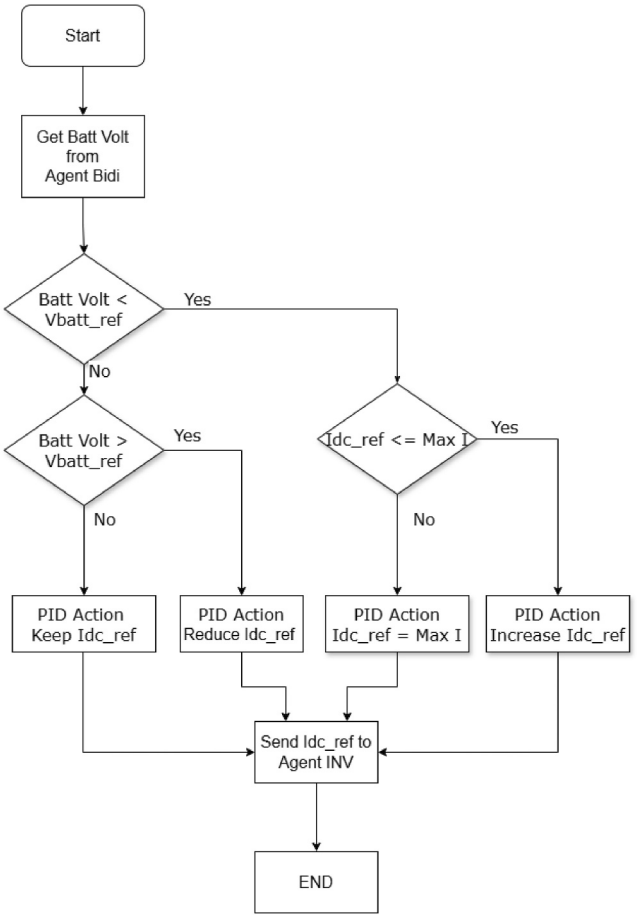

FIGURE 10 | Control algorithm flowchart for the MAS.

In this flowchart, the variable V_{batt_ref} stores the battery voltage reference according to the system setup, whereas *Idc_ref* represents the inverter/rectifier control reference for the direct axis current (*Id*) [17]. Primary control logic resides within each converter in a hierarchical and distributed architecture [18], featuring faster response times than the MAS's secondary control. The MAS incorporates a PID controller at this secondary layer comparing the actual battery voltage to a predefined reference of 720 VDC. Its output determines the current required by the inverter (INV), which either supplies power to the DC bus or exports excess energy to the grid. The PV unit operates in MPPT mode and may produce surplus energy depending on solar irradiance.

Figure 11 illustrates the hierarchical control structure adopted in this work, highlighting the two-layer architecture and associated update rates. The lower layer comprises local controllers embedded in each simulator (PSIM, PLECS and RTDS), operating at high-frequency steps to capture fast converter dynamics: 20 μs for PV and consumer-side inverters (PSIM), up to 1 ms for the bidirectional DC/DC converter (PLECS) and 50 μs for the grid interface converter (RTDS). These controllers ensure accurate modelling of electrical transients and primary control actions. The upper layer corresponds to the MAS, implemented in Python and communicating asynchronously via TCP/IP sockets. This supervisory layer executes secondary control tasks, including battery voltage regulation (used as a proxy for SoC) and grid interaction, at an adaptive update rate ranging from 30–70 Hz (average ≈35 Hz, ≈28.6 ms per cycle), dynamically adjusted according to network conditions. The figure also emphasises the nonblocking communication strategy: simulators continue their internal steps independently while exchanging measurements and commands with the MAS, preventing synchronisation bottlenecks and ensuring responsiveness across heterogeneous platforms. This configuration reflects the time-domain separation between fast local dynamics (μs–ms) and slower supervisory actions (tens of ms), enabling the co-simulation framework to integrate real-time and non-real-time environments under varying communication scenarios.

Beyond coordinating control actions, the MAS ensures synchronisation among heterogeneous simulators operating under different execution profiles (real-time and non-real-time). This

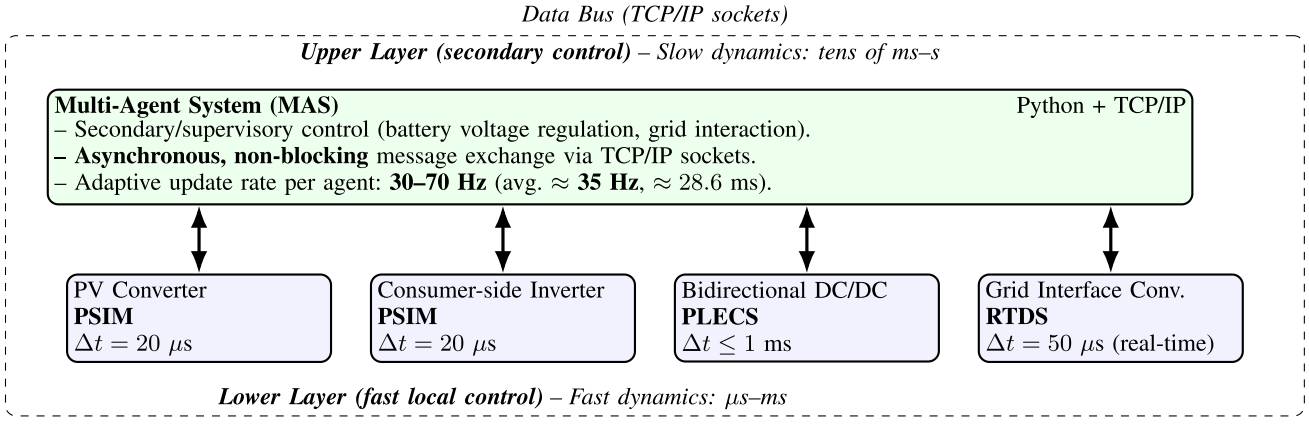

FIGURE 11 | Heterogeneous simulators (lower layer) exchange measurements and commands with a multiagent system (upper layer) via asynchronous, nonblocking TCP/IP. Per-agent adaptive update rate: 30–70 Hz (avg. ≈35 Hz).

25152947, 2026, 1, Downloaded from https://ietresearch.onlinelibrary.wiley.com/doi/10.1049/stg2.70054 by Uppsala University Library, Wiley Online Library on [04/08/2026]. See the Terms and Conditions (https://onlinelibrary.wiley.com/terms-and-conditions) on Wiley Online Library for rules of use; OA articles are governed by the applicable Creative Commons License

capability is critical for maintaining stability in the proposed co-simulation environment. Additionally, the MAS implements the adaptive update rate algorithm described in Section 2.3, dynamically adjusting communication frequency based on observed network conditions. This mechanism allows the system to remain with the desired performance even under degraded communication scenarios, where delays or packet retransmissions may occur. These features collectively demonstrate the MAS's ability to guarantee reliable operation in strongly heterogeneous and adverse communication environments.

2.5 | System Architecture

Figure 12 illustrates the system architecture, showing how the components are interconnected. The diagram identifies two separate buses: one for power transmission and another for data communication. The power bus physically connects the power converters and the grid, enabling energy flow. The data bus supports communication between the system's components, for instance, between the agents (communication-enabled converters) and the MAS. TCP/IP socket communication is used throughout the network. In the Figure 12, one may see some converters as described in Section 2.2:

- Buck PV (PV);
- Bidi (bidirectional);
- Inverter (inverter/rectifier);
- Consumer (consumer-side).

The PCC (point of common coupling) represents the interface between the microgrid and the main grid. Measurements collected throughout the system are obtained from sensors positioned at key locations as detailed in Table 4.

Where:

- V_{Bus} is the measured DC bus voltage;
- I_{PV} is the current generated by the PV panel converter;
- I_{INV} is the current supplied to or drawn from the DC bus by the inverter/rectifier (INV);
- I_{Load} is the current consumed by the system load;
- I_{Bus} is the current measured at the DC bus;
- I_{Bat} is the battery current (charge or discharge);
- V_{RMS} is the RMS voltage measured at the inverter-grid connection.

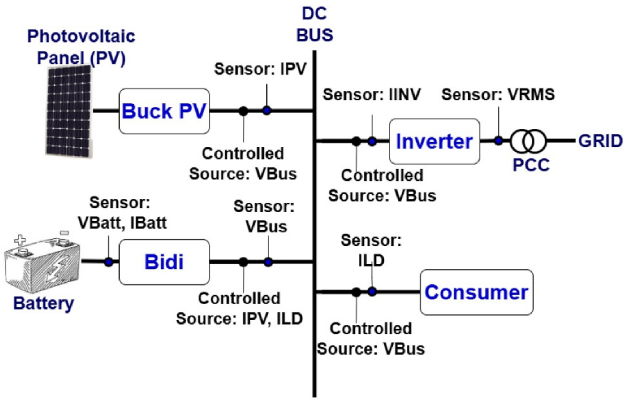

FIGURE 12 | System architecture.

From Equation (12), the nominal storage capacity of the battery is given by $Q_{nominal} = 10.9\ kAs$, which is obtained through a current drained from the system battery of $i = 40\ A$. The current was drained through a resistor of $R = 18\ \Omega$ with an initial battery voltage of $V_{bus} = 720\ V$ within a period of 429 s. The capacitor value is set to $C = 24\ F$. The PV array provides 40 A when the solar irradiance is 1 kWh/m^2

$$Q_{nominal} = \frac{V_{bus}}{R} \times \int_0^{\tau} e^{-\frac{\tau}{RC}}, dx. \tag{12}$$

The energy is given by Equation (13) as follows:

$$E = Q_{nominal} \times V_{bus}\ J. \tag{13}$$

Finally, replacing $Q_{nominal}$ From Equation (12), the battery capacity in kWh is given by

$$\begin{aligned} E &= 10.9\ k\ \mathrm{C} \times 900\ V \\ &= 9,810,000\ \mathrm{J} \\ &= 2.725\ kWh. \end{aligned} \tag{14}$$

3 | Results

The experimental results demonstrate the system's capability to maintain both the DC bus voltage (900 V), controlled by bidirectional converter and battery voltage level (720 V), controlled by MAS. Figure 13 displays the physical elements of the system along with their corresponding computer station identifications. The detailed configurations of the computers that supported the solvers can be found in Table 5. Network equipment consist of a switch and a router physically connecting system elements.

Table 6 lists the corresponding hardware for each subsystem element for simulation.

Figure 14, generated from the PostgreSQL database logs, presents the system behaviour over a 500 s simulation period. The sequence of sub-figures illustrates the electrical and communication performance of the proposed distributed control architecture.

TABLE 4 | System variable description.

Converter	Controlled source	Sensor	Reference
Buck PV	V_{Bus}	I_{PV}	MPPT
Bidi	I_{PV}, I_{INV}, I_{Load}	V_{Bus}, I_{Bus}, I_{Bat}	V_{Bus}
Inverter/ rectifier	V_{Bus}	I_{INV}, V_{RMS}	I_{Bus}
Load	V_{Bus}	I_{Load}	—

25152947, 2026, 1, Downloaded from https://ietresearch.onlinelibrary.wiley.com/doi/10.1049/stg2.70054 by Uppsala University Library, Wiley Online Library on [04/08/2026]. See the Terms and Conditions (https://onlinelibrary.wiley.com/terms-and-conditions) on Wiley Online Library for rules of use; OA articles are governed by the applicable Creative Commons License

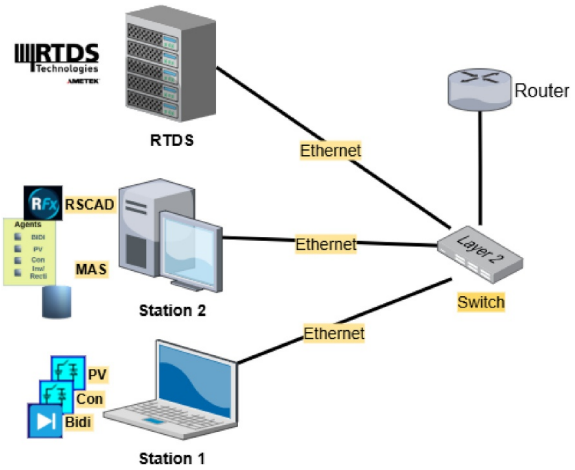

FIGURE 13 | Co-simulator system physical elements.

TABLE 5 | Hardware used in the experiment.

Name	Processor	Clk speed	RAM
RTDS	PB5, GTNET and GPC	Real time	—
Station 1	Intel(R) Core(TM) *i*5-1135*G*7	2.40 *GHz*	8.00*GB*
Station 2	Intel(R) Core(TM) *i*7-3770	3.40 *GHz*	24.0*GB*

TABLE 6 | Hardware versus subsystem element.

Hardware	Solvers
RTDS	Inverter/rectifier
Station 1	Bidi, PV and Con
Station 2	RSCAD, multiagent system and database

Figure 14a shows the voltage profiles of the DC bus and the battery. The control system successfully maintains the DC bus voltage (V_{Bus}) at approximately 900 V and the battery voltage (V_{Batt}) near its nominal value of 720 V. These results confirm the effectiveness of the hierarchical control structure in stabilising the voltage under both nominal and disturbed operating conditions. Minor fluctuations are rapidly corrected, demonstrating adequate response from both local and supervisory controllers.

The current dynamics, presented in Figure 14b, include four key variables: the INV current (I_{Inv}), the photovoltaic converter current (I_{PV}), the consumer load current (I_{Con}) and the battery current (I_{Batt}). At $t = 28$ s, a sharp increase in consumption, reflected in I_{Con}, of approximately 260% occurs, simulating a sudden load demand. The bidirectional converter responds immediately by injecting current from the battery, whereas a slight voltage dip in V_{Batt} is detected and corrected by the MAS. The secondary control-loop implemented via a PID controller adjusts the INV's current reference, leading to a gradual increase in power injection from the grid. Later, at $t = 180$ s, an increase in solar irradiance causes I_{PV} to rise from 10 to 35 A. The MPPT algorithm ensures maximum energy production, whereas the MAS reduces INV injection to prevent overvoltage, preserving voltage stability across the system.

The power output of the inverter/rectifier (INV) at the DC Bus is shown in Figure 14c. The plot illustrates the temporal variation

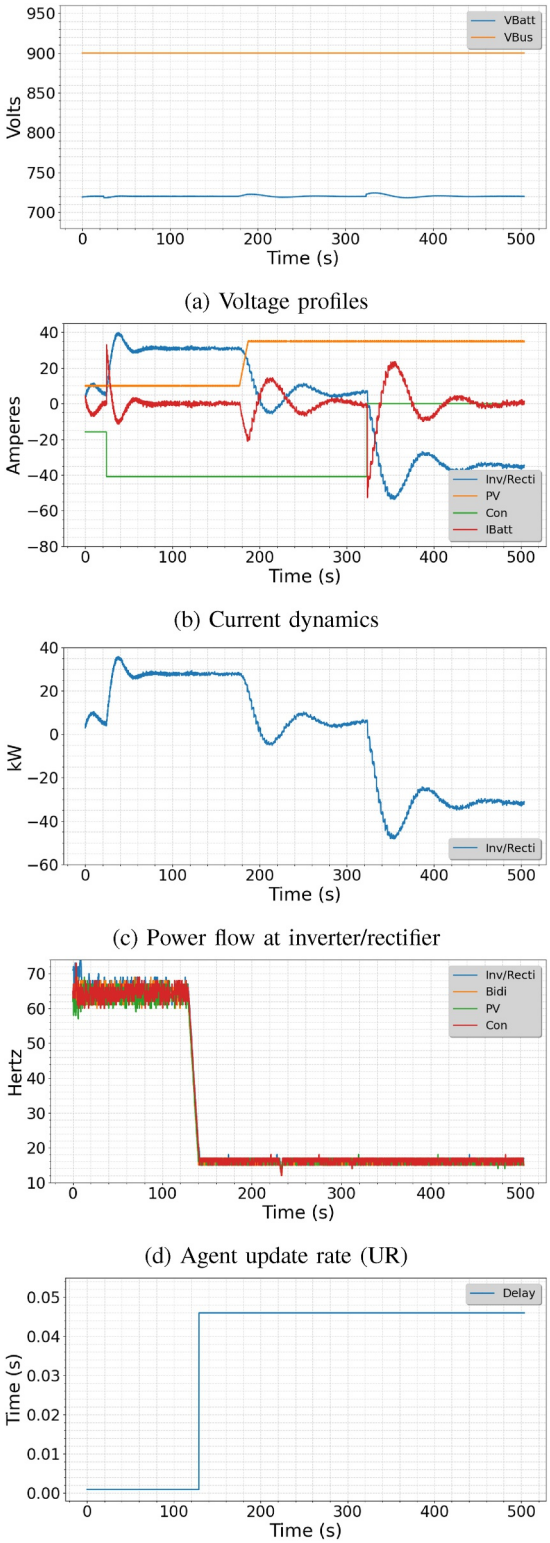

(a) Voltage profiles

(b) Current dynamics

(c) Power flow at inverter/rectifier

(d) Agent update rate (UR)

(e) Communication channel delay

FIGURE 14 | System performance metrics over a 500-s window.

in the power exchanged with the external grid. A reversal in power flow direction was observed during the simulation period, indicating that the INV dynamically adjusted its power exchange to respond to fluctuations in local generation and demand, as affected by changes in PV, load and battery behaviour.

25152947, 2026, 1, Downloaded from https://ietresearch.onlinelibrary.wiley.com/doi/10.1049/stg2.70054 by Uppsala University Library, Wiley Online Library on [04/08/2026]. See the Terms and Conditions (https://onlinelibrary.wiley.com/terms-and-conditions) on Wiley Online Library for rules of use; OA articles are governed by the applicable Creative Commons License

Positive values in Figure 14c (above 0 kW) indicate that the grid is supplying energy to the microgrid, whereas negative values signify that the microgrid is exporting energy to the grid. Summarising its operation, during the 500 s simulation period, the main grid supplied energy to the microgrid for 61% of the total time. Conversely, for the remaining 39%, the microgrid exported energy back to the main grid. This bidirectional power flow highlights the effectiveness of the distributed control strategy in regulating grid interaction. It ensures a coordinated and stable power exchange, prevents overloading and provides adequate support for maintaining voltage stability across the DC bus. Table 7 lists the system elements rated capacity.

Figure 14d illustrates the evolution of the update rate (UR) for each agent as regulated by the adaptive algorithm described earlier. Notably, around $t = 120$ s, a reduction in UR is applied to certain agents in response to the transient event, likely driven by increased message processing times and network congestion. As communication stabilises, the update periods are gradually restored to nominal levels. This behaviour demonstrates the MAS's ability to adjust communication frequency to avoid overload and preserve responsiveness.

Finally, Figure 14e reports the communication delay parametrised in the simulator—at Python layer—between agents and the MAS. The NS-3 simulation script `wifi-spectrum-per-example.cc` [19] was executed in order to substantiate the referred delay using the parameters listed in Table 8.

A significant increase in round-trip time (RTT) is observed when packet retransmissions occur. Under normal operating conditions, RTT values were found around 0.84 ms. However, in scenarios with packet retransmissions, RTT can reach up to 55.3 ms. The final delay value was simulated at 46.0 ms from instant 130 s. This spike aims to simulate a momentary saturation of the communication channel and demonstrates the impact of retransmissions on communication latency within the network, evidencing how network conditions can interfere with the systems' performance [20]. Despite this temporary degradation, no loss of synchronisation occurred. This resilience is attributed to the deterministic sequencing of messages by the MAS server and the adaptive reduction of update rates. Together, these mechanisms ensure reliable system performance even under adverse network conditions.

TABLE 7 | System elements rated capacity.

Element	Unit	Value
PV	kW	45.0
Bidi	kW	45.0
Battery	kWh	2.725
Cons	kW	36.0
INV	kW	54.0

TABLE 8 | Parameters used in the NS-3 simulation session.

Parameter	Value
WiFi type	ns3::SpectrumWifiPhy
Distance	50 m
Transmission power	1 dBm (1.3 mW)
Data rate	7.2 Mb/s
Throughput	5 Mb/s
Channel bandwidth	20 MHz
Signal strength	−79.74 dBm
Noise level	−93.97 dBm

Figure 15 illustrates the scenario in which the current generated by the PV array decreases due to a simulated reduction in solar irradiance occurred in the instant $t = 128\ s$ where the PV output falls from 40 A to 12 A. In response to MAS coordination, the inverter shifts the state of microgrid from energy equilibrium to importing power from the main grid.

Figure 16 illustrates the scenario in which the microgrid operates under a fixed update rate, used as a benchmark for comparison with the one discussed in Figure 14. The same communication network parameters presented in Table 8 were applied in this scenario as a baseline for selecting the communication medium delay. A fixed update rate of 30 Hz was selected as a representative operating point, suitable for capturing the system dynamics related to communication delays both before and after a step change as illustrated in Figure 16c. Figure 16a shows the voltage behaviour over a 500 s time window, where the V_{Batt} and V_{Bus} waveforms remain stable before and after the change in the communication network conditions. Figures 14b and 16b, respectively, illustrate the adaptive and fixed update rate scenarios, which are compared in terms of their settling times following a sudden load variation. A change in consumer load triggers an immediate response from the battery, T1 and T2 in Table 9, whereas the inverter (INV) requires the time intervals to reach its new steady-state operating points, ST1 and ST2, between the 5% operating margin. These settling times reflect the coordination delay introduced by the MAS when operating under adaptive and fixed update rates. Based on the ratio between the settling times before and after the communication medium delay variation in both scenarios, it is important to note that the DC bus voltage remains stable. Table 9 summarises the observed settling times for both methods, listing in the column *Average* the settling times variation average between events occurring before and after the communication delay conditions change, represented by T1 and T2.

Overall, the results demonstrate that the adaptive update rate strategy provides superior dynamic performance compared to

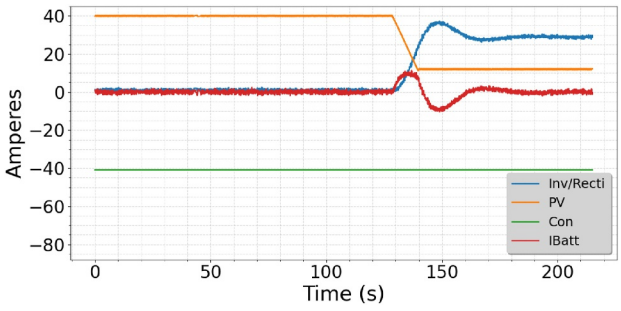

FIGURE 15 | A solar irradiance occurs lowering the PV converter output.

25152947, 2026, 1, Downloaded from https://ietresearch.onlinelibrary.wiley.com/doi/10.1049/stg2.70054 by Uppsala University Library, Wiley Online Library on [04/08/2026]. See the Terms and Conditions (https://onlinelibrary.wiley.com/terms-and-conditions) on Wiley Online Library for rules of use; OA articles are governed by the applicable Creative Commons License

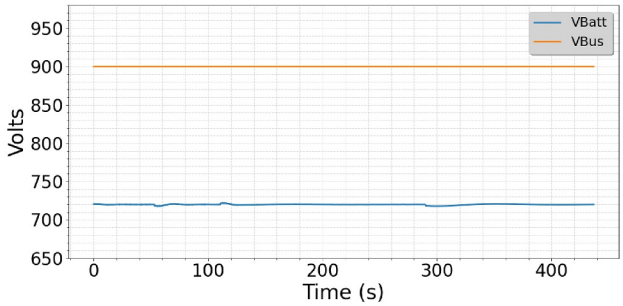

(a) Voltage profiles.

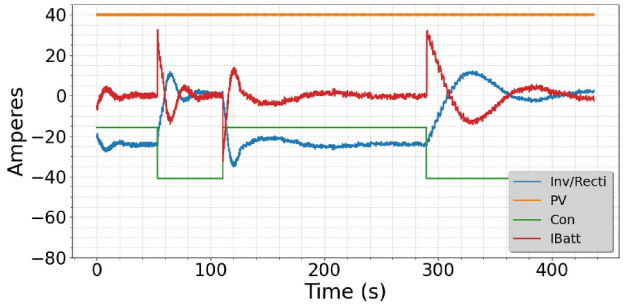

(b) Current profiles.

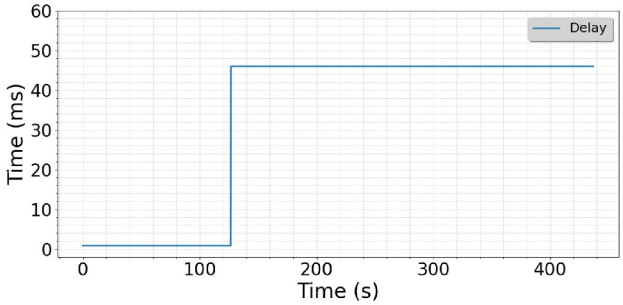

(c) Communication channel delay profile, defined based on the NS-3 simulation.

FIGURE 16 | System operating under fixed update rate.

TABLE 9 | Comparison between adaptive and fixed update rates.

Method	T1 (s)	ST1 (s)	T2 (s)	ST2 (s)	Average
Adaptive	29	32.8	327	432	232.4 *s*
Fixed	53	104	289	430	267 *s*

the fixed update rate benchmark. Although both approaches maintain voltage and current stability, the adaptive method significantly reduces the settling time average throughout the operation were occurs transient events, ensuring faster coordination between agents and improved responsiveness of the inverter and battery systems. By dynamically adjusting communication frequency under varying network conditions, including degraded scenarios, the proposed approach mitigates the impact of delays and enhances the efficiency of distributed control in hybrid microgrid environments.

4 | Conclusion

The proposed distributed control system demonstrated its effectiveness in maintaining DC bus voltage and battery state of charge (SoC) within a heterogeneous co-simulation environment that integrates real-time simulators (RTDS) and non-real-time platforms (PLECS and PSIM). This integration reflects real-world operational challenges and validates the capability of the multi-agent system (MAS) to coordinate components across platforms with different execution profiles while ensuring system stability.

A key contribution of this work is the implementation of an adaptive update rate strategy, which dynamically adjusts communication frequency based on network conditions. Experimental results showed that this approach significantly improves the dynamic performance of the system compared to a fixed update rate benchmark. Although both strategies ensured voltage stability, the adaptive method reduced settling time during transients, enabling faster coordination between agents and more responsive inverter and battery control. Furthermore, the adaptive algorithm proved capable of mitigating the impact of degraded communication scenarios, maintaining reliable operation even under increased latency and packet retransmissions.

These findings confirm that adaptive communication control is a critical enabler for distributed control in hybrid microgrid environments.

Author Contributions

Daniel Leocádio Fernandes: conceptualisation, formal analysis, investigation, methodology, software, validation, writing – original draft, writing – review and editing. **Guilherme Márcio Soares:** conceptualisation, data curation, formal analysis, methodology, resources, supervision, validation, writing – original draft, writing – review and editing. **Janaína Gonçalves de Oliveira:** conceptualisation, formal analysis, funding acquisition, methodology, resources, supervision, writing – review and editing.

Acknowledgements

The authors would like to thank the financial support of CAPES (Funding Code 88887.799837/2022-00).

Conflicts of Interest

The authors declare no conflicts of interest.

Data Availability Statement

Data sharing is not applicable to this article as no datasets were generated or analysed during the current study.

References

1. D. Kumar, F. Zare, and A. Ghosh, "DC Microgrid Technology: System Architectures, AC Grid Interfaces, Grounding Schemes, Power Quality, Communication Networks, Applications, and Standardizations Aspects," *IEEE Access* 5 (2017): 12230–12256, https://doi.org/10.1109/ACCESS.2017.2705914.

2. J. H. Kazmi, A. Latif, I. Ahmad, P. Palensky and W. Gawlik, "A Flexible Smart Grid Co-Simulation Environment for Cyber-Physical Interdependence Analysis," 2016 Workshop on Modeling and Simulation of Cyber-Physical Energy Systems (MSCPES), Vienna, Austria, 2016, 1–6, https://doi.org/10.1109/MSCPES.2016.7480226.

3. M. Azeroual, Y. Boujoudar, L. E. Iysaouy, et al., "Energy Management and Control System for Microgrid Based Wind-PV-Battery Using

25152947, 2026, 1, Downloaded from https://ietresearch.onlinelibrary.wiley.com/doi/10.1049/stg2.70054 by Uppsala University Library, Wiley Online Library on [04/08/2026]. See the Terms and Conditions (https://onlinelibrary.wiley.com/terms-and-conditions) on Wiley Online Library for rules of use; OA articles are governed by the applicable Creative Commons License

Multi-Agent Systems," *Wind Engineering* 46, no. 4 (2022): 1247–1263, https://doi.org/10.1177/0309524X221075583.

4. S. Majumder, A. Vosughi, H. M. Mustafa, T. E. Warner, and A. K. Srivastava, "On the Cyber-Physical Needs of DER-Based Voltage Control/Optimization Algorithms in Active Distribution Network," *IEEE Access* 11 (2023): 64397–64429, https://doi.org/10.1109/access.2023.3278281.

5. M. T. Le, T. L. Nguyen, Q. T. Tran, Y. Besanger, and T. T. Hoang, "A Co-Simulation Approach for Validating Agent-Based Distributed Algorithms in Smart Grid," in *2020 IEEE 20th Mediterranean Electrotechnical Conference (MELECON)* (IEEE, 2020), 529–534, https://doi.org/10.1109/MELECON48756.2020.9140496.

6. R. Rana, K. Berg, M. Z. Degefa, and M. Loschenbrand, "Modelling and Simulation Approaches for Local Energy Community Integrated Distribution Networks," *IEEE Access* 10 (2022): 3775–3789, https://doi.org/10.1109/ACCESS.2022.3140237.

7. R. E. Perez Guzman, M. Rivera, P. W. Wheeler, G. Mirzaeva, E. E. Espinosa, and J. A. Rohten, "Microgrid Power Sharing Framework for Software Defined Networking and Cybersecurity Analysis," *IEEE Access* 10 (2022): 111389–111405, https://doi.org/10.1109/ACCESS.2022.3215434.

8. A. D'Elia, F. Viola, F. Montori, et al., "Impact of Interdisciplinary Research on Planning, Running, and Managing Electromobility as a Smart Grid Extension," *IEEE Access* 3 (2015): 2281–2305, https://doi.org/10.1109/ACCESS.2015.2499118.

9. C. Shum, W. H. Lau, T. Mao, et al., "DecompositionJ: Parallel and Deterministic Simulation of Concurrent Java Executions in Cyber-Physical Systems," *IEEE Access* 6 (2018): 21991–22010, https://doi.org/10.1109/ACCESS.2018.2825254.

10. Y. Litman, V. Kapil, Y. M. Y. Feldman, et al., "i-PI 3.0: A Flexible and Efficient Framework for Advanced Atomistic Simulations," *Journal of Chemical Physics* 161, no. 6 (August 14, 2024): 062504, https://doi.org/10.1063/5.0215869.

11. M. Dold, J. Pereira, B. Sajonz, et al., "Dareplane: A Modular Open-Source Software Platform for BCI Research With Application in Closed-Loop Deep Brain Stimulation," *Journal of Neural Engineering* 22, no. 2 (2025): 026029, https://doi.org/10.1088/1741-2552/adbb20.

12. M. S. Alam, M. A. Hossain, M. Shafiullah, et al., "Renewable Energy Integration With DC Microgrids: Challenges and Opportunities," *Electric Power Systems Research* 234 (2024): 110–548, https://doi.org/10.1016/j.epsr.2024.110548.

13. RTDS Technologies Inc, *RTDS Simulator* (RTDS Technologies Inc., 2024), https://www.rtds.com/.

14. OSI, "Open Systems Interconnection Model,", http://www.iso.org.

15. ns-3 Consortium, "NS-3: A Discrete-Event Network Simulator," 2023, https://www.nsnam.org/.

16. A. S. Tanenbaum and M. Van Steen, *Distributed Systems: Principles and Paradigms*. 2nd ed. (Prentice Hall, 2007).

17. A. Yazdani and R. Iravani, *Voltage-Sourced Converters in Power Systems: Modeling, Control, and Applications* (IEEE Press, 2010).

18. D. Y. Yamashita, I. Vechiu, and J.-P. Gaubert, "A Review of Hierarchical Control for Building Microgrids," *Renewable and Sustainable Energy Reviews* 118 (2020): 109523, https://doi.org/10.1016/j.rser.2019.109523.

19. M. Banchi, S. Deronne, and T. Henderson, "NS-3 Consortium,", https://www.nsnam.org/.

20. D. L. Fernandes, A. L. M. Leopoldino, J. de Santiago, C. Verginis, A. A. Ferreira, and J. G. de Oliveira, "Distributed Control on a Multi-Agent Environment Co-Simulation for DC Bus Voltage Control," *Electric Power Systems Research* 232 (2024): 110408, https://doi.org/10.1016/j.epsr.2024.110408.

25152947, 2026, 1, Downloaded from https://ietresearch.onlinelibrary.wiley.com/doi/10.1049/stg2.70054 by Uppsala University Library, Wiley Online Library on [04/08/2026]. See the Terms and Conditions (https://onlinelibrary.wiley.com/terms-and-conditions) on Wiley Online Library for rules of use; OA articles are governed by the applicable Creative Commons License